REFERENCES AND NOTES

1. R. W. Simpson, S. S. Schulz, L. D. Dietz, R. O. Burford, *Pure Appl. Geophys.* **126**, 665 (1988).
2. Working Group on California Earthquake Probabilities, *U.S. Geol. Surv. Circ.* **1053**, 51 (1990).
3. J. J. Lienkaemper, G. Borchardt, M. Lisowski [*J. Geophys. Res*. **96**, 18261 (1991)], being revised as J. J. Lienkaemper and J. S. Galehouse, in preparation; J. J. Lienkaemper, J. S. Galehouse, R. W. Simpson, *Eos* **73**, 119 (1992); ———, K. S. Breckenridge, *ibid.* **74**, 192 (1993).
4. P. A. Reasenberg and R. W. Simpson, *Science* **255**, 1687 (1992).
5. R. W. Simpson and P. A. Reasenberg, *U.S. Geol. Surv. Prof. Pap*. **1550-F**, 55 (1994).
6. J. S. Galehouse, *Geophys. Res. Lett.* **17**, 1219 (1990); *U.S. Geol. Surv. Prof. Pap*., in press.
7. ———, B. D. Brown, B. Pierce, J. J. Thordsen, *Calif. Div. Mines Geol. Spec. Publ.* **62**, 239 (1982).
8. J. Langbein and H. Johnson, *J. Geophys. Res*. **102**, 591 (1997).
9. J. C. Savage and M. Lisowski, *ibid*. **98**, 787 (1993).
10. The previous largest event on the fault was 10 mm in 1983 during a 124-day interval at km 62. The date of the 18-mm event may be 9 February 1996, when a water main broke at km 65.9 on the fault. This 1996 event extended more than 1.7 km (from km 65.3 to 67.0), as shown on four arrays but less than 3.7 km, as limited by other data. We observed no triggered slip on the Hayward fault in 1989 except for 3 mm that showed on fresh cracks at km 66.3 (*3*).
11. Suddenness of resumption of fast creep from km 65 to 67 may be caused by two extremely rainy seasons following a drought. North of km 63, all sites had resumed pre–Loma Prieta rates by 1994. Two sites, km 63 and 64, resumed nearly normal rates during 1994. A creepmeter at km 63.6 resumed a 9 mm/year rate by late 1995 with no large event in early 1996. We note that a borehole strainmeter located 5 km northeast of the ~18-mm creep event recorded a strain event starting on 7 February 1996. These data are consistent with slip of 18 mm on a patch ~1 km in extent (M. Johnston, personal communication). Possibly, creep began steadily at depth months earlier, not slipping at the surface until induced by a water table raised by heavy rains.
12. M. Lisowski, W. H. Prescott, J. C. Savage, M. J. Johnston, *Geophys. Res. Lett.* **17**, 1437 (1990). Dislocation model parameters: 37 km in length; 316° strike, 70°SW dip; depth of 5 to 17.5 km; 1.66-m dextral slip; and 1.19-m reverse. Other models tested yield similar results for the Hayward fault (*4, 5*).

13. Funded by the U.S. Geological Survey National Earthquake Hazards Reduction Program (NEHRP) and San Francisco State University (NEHRP contract 1434-94-G2420). We thank many student assistants, especially C. Garrison, O. Graves, T. Hoyt, and F. McFarland; the governments of Fremont, Hayward, San Leandro, and Oakland; W. Hazelwood of the Bay Area Rapid Transit District; D. J. Russell; and two anonymous reviewers, W. Prescott and J. Langbein.

11 March 1997; accepted 5 May 1997

Single Polymer Dynamics in an Elongational Flow

Thomas T. Perkins, Douglas E. Smith, Steven Chu*

The stretching of individual polymers in a spatially homogeneous velocity gradient was observed through use of fluorescently labeled DNA molecules. The probability distribution of molecular extension was determined as a function of time and strain rate. Although some molecules reached steady state, the average extension did not, even after a ~300-fold distortion of the underlying fluid element. At the highest strain rates, distinct conformational shapes with differing dynamics were observed. There was considerable variation in the onset of stretching, and chains with a dumbbell shape stretched more rapidly than folded ones. As the strain rate was increased, chains did not deform with the fluid element. The steady-state extension can be described by a model consisting of two beads connected by a spring representing the entropic elasticity of a worm-like chain, but the average dynamics cannot.

The behavior of dilute polymers in elongational flow has been an outstanding problem in polymer science for several decades (*1, 2*). In elongational flows, a velocity gradient along the direction of flow can stretch polymers far from equilibrium. Extended polymers exert a force back on the solvent that leads to the important, non-Newtonian properties of dilute polymer solutions, such as viscosity enhancement and turbulent drag reduction.

A homogeneous elongational flow is defined by a linear velocity gradient along the direction of flow such that $v_y = \dot{\varepsilon}y$, where $\dot{\varepsilon} \equiv \partial v_y/\partial y$, the strain rate, is constant. Theory suggests that the onset of polymer stretching occurs at a critical velocity gradient or strain rate of $\dot{\varepsilon}_c$ of

$$\dot{\varepsilon}_c \approx \frac{0.5}{\tau_1} \qquad (1)$$

where τ_1 is the longest relaxation time of the polymer (*3*). For $\dot{\varepsilon} < \dot{\varepsilon}_c$, the molecules are in a "coiled" state. But as $\dot{\varepsilon}$ is increased above $\dot{\varepsilon}_c$, the hydrodynamic force exerted across the polymer just exceeds the linear portion of the polymer's entropic elasticity, and the polymer stretches until its nonlinear elasticity limits the further extension of this "stretched" state. De Gennes predicted that this "coil-stretch transition" would be sharpened by an increase in the hydrodynamic drag of the stretched state relative to the drag of the coiled state (*1*).

In many types of elongational flows, such as flow through a pipette tip, the residency time t_{res} of the polymers in the velocity gradient is limited. To increase t_{res}, flows in which there is a stagnation point are often used. As molecular trajectories approach the stagnation point, t_{res} diverges. The classical techniques for inferring the degree of polymer deformation have been light scattering (*4, 5*) and birefringence (*6–9*). For example, Keller and Odell reported a rapid increase in the birefringence for $\dot{\varepsilon}$ above $\dot{\varepsilon}_c$ followed by a saturation (*6*). Such saturation was interpreted as an indication that the polymers had reached equilibrium in a highly extended state (*10*). Molecular weight analysis showed some chains are fractured in half, further supporting the hypothesis that the polymers reached full extension (*8, 11*). However, light-scattering experiments imply deformations of only two to four times the equilibrium size (*4, 5*). But, these "bulk" measurements average over a macroscopic number of molecules with a broad range of t_{res}. Moreover, only recent experiments have been dilute enough to prevent the polymers from altering the flow field (*9*).

Many rheological effects also remain unexplained. James and Saringer measured a pressure drop in a converging flow that was significantly greater than that predicted by simple models (*12*). Recently, Tirtaatmadja and Sridhar measured extensional viscosities η_E in filament stretching experiments that were several thousand times greater than the shear viscosities (*13*). At large deformations, η_E saturated, suggesting again that the polymers were fully extended. However, the measured stress was significantly lower than expected for fully extended polymers, implying that full extension had not actually been achieved (*14*). Also, the stress relaxation in such experiments contained both a strain-rate independent "elastic" and a strain-rate dependent "dissipative" component. The molecular origin of the dissipative component is uncertain (*15*). Examples such as these indicate that, even after a tremendous amount of study, the deformation of polymers in elongational flows is still poorly understood (*14, 16*).

We report the direct visualization of individual polymers in an elongational flow. The conformation and extension of each molecule was measured as a function of $\dot{\varepsilon}$ and t_{res}, thereby eliminating the ambiguities in conformation and t_{res}. We further eliminated polymer-polymer interactions and polymer-induced alterations of the flow field by working with single isolated molecules. The inherent uniformity

Department of Physics, Stanford University, Stanford, CA 94305, USA.

*To whom correspondence should be addressed. E-mail: schu@leland.stanford.edu

in size of lambda bacteriophage DNA [λ-DNA, $L_{strained} \cong 22$ μm (*17*)] also eliminated complications due to polydispersity and enabled accurate calculation of ensemble averages (*18*). Thus, we determined the probability distribution of molecular extension rather than just an average or a moment of that distribution. Another advantage is that the entropic elasticity (*19, 20*) and hydrodynamic drag (*17, 21, 22*) of single DNA molecules have been previously characterized.

Using a microfabricated flow cell, we generated a planar elongational flow with a cross-slot geometry adapted for fluorescence microscopy (*23*). The main design consideration of the flow cell was to ensure that we studied dynamics of polymers unwinding from equilibrium (*24*). Our imaging area was 100 μm by 94 μm with the stagnation point 15 μm from the center of one side. The onset of the elongational flow, where $t_{res} = 0$, was 960 μm up the inlet channel from the stagnation point.

By tracking individual molecules, we measured the extension x and t_{res} of each molecule in our imaging area. Some molecules deformed only slightly, whereas others rapidly reached a steady-state extension (Fig. 1A). This large and previously unobservable heterogeneity was perhaps unexpected because these molecules were identical in size and had experienced the same $\dot{\varepsilon}$ and t_{res}. From an ensemble of individual measurements, we calculated the average extension $\langle x(t_{res})\rangle$ as well as the time evolution of the probability distribution for molecular extension (Fig. 1B).

We characterized the conformation of each polymer in the ensemble. In general, the molecules were found in one of seven conformations which we refer to as dumbbell, half-dumbbell, folded, uniform, kinked, coiled, or extended. The first three types were dominant at $\dot{\varepsilon} = 0.86\ s^{-1}$. As shown in Fig. 2A, these are highly nonequilibrium conformations, and they occurred only at higher strain rates ($\dot{\varepsilon} > 0.5\ s^{-1}$) (*25*). In this case, the molecules were subject to a $\dot{\varepsilon}$ significantly greater than the inverse relaxation time [$\tau_{relax}^{-1} = 0.26$; $\tau_{relax} = 3.89$ s (*26*)]. For λ-DNA (~400 persistence lengths), we saw only single folds at the highest $\dot{\varepsilon}$ investigated. However, for longer molecules, we observed multiple folds (*27*).

There were clear differences in dynamics for the three dominant conformations. To highlight these differences, we plotted data, using only those molecules that best typified each conformational class. Molecules in a dumbbell configuration stretched significantly faster than folded ones (Fig. 2B). In addition, the residency time t_{onset} at which significant stretching begins for any particular molecule was highly variable (*28*).

An analysis of the rate of stretching $\dot{x}$ as function of x shows that once a molecule in a dumbbell configuration starts to stretch, its dynamics follows a specific time evolution (Fig. 2C, inset). This result indicates that the data would approximately collapse onto a single "master curve" by sliding the individual curves along the time axis. Up to $x/L = 0.6$, we observed a linear increase in $\langle \dot{x}(x)\rangle$ with x up to $x = 12$ μm at $\dot{\varepsilon} = 0.86\ s^{-1}$. When integrated, this yields an initial exponential growth of the master curve. We show three such master curves generated from the molecules that best typify each of the dominant conformations (Fig. 2C). For comparison, we show $\langle x(t_{res})\rangle$ for the full data set as well as for several of the different conformational classes arising from the first, general classification (Fig. 2D). Because of the large variation in t_{onset}, the master curve better represents the unwinding dynamics of individual molecules and is different in shape than $\langle x(t_{res})\rangle$.

We plotted the fractional average extension $\langle x\rangle/L$ as a function of the accumulated fluid strain or "Henky stain" ($\varepsilon = \dot{\varepsilon} t_{res}$) (Fig. 3A). By analyzing the subset of molecules that reached steady state (Fig. 3B, inset), we determined the steady-state extension x_{steady} as a function of the dimensionless strain rate or "Deborah number" $\dot{\varepsilon}\tau_{relax}$ (Fig. 3B). Note that x_{steady} rises sharply at a critical strain rate of $\dot{\varepsilon}_c\tau_{relax} \cong 0.4$ and that for $\dot{\varepsilon} \cong 0.9\ \dot{\varepsilon}_c$ the fractional size of fluctuations is large ($\sigma_x / x_{steady} \cong 0.4$). Similar behavior is often seen at phase transitions. In comparison with classical bulk measurements, we also plotted a spatio-temporal average x_{bulk} of all our data (Fig. 3B).

In a linear velocity-gradient flow ($\dot{\varepsilon}_{fluid} \equiv \dot{\varepsilon} = \partial v_y/\partial y$), the distance between two fluid elements grows as $y \sim \exp(\dot{\varepsilon}_{fluid} t_{res})$. There was a similar but slower exponential growth in the master curves of molecular extension for $\dot{\varepsilon} > 0.21\ s^{-1}$. We defined a molecular strain rate $\dot{\varepsilon}_{mol}$ from a fit of $\langle \dot{x}(x)\rangle = \dot{\varepsilon}_{mol}\, x + b$ over the region where $\langle \dot{x}(x)\rangle$ is a linear function of x (Fig. 4, inset) and compared $\dot{\varepsilon}_{mol}$ to $\dot{\varepsilon}_{fluid} - \dot{\varepsilon}_c$ (Fig. 4). This analysis averages over the conformation-dependent dynamics shown in Fig. 2. To single out the most rapid stretching conformation, we also plotted $\dot{\varepsilon}_{mol}$ for the dumbbell configuration at $\dot{\varepsilon} = 0.86\ s^{-1}$.

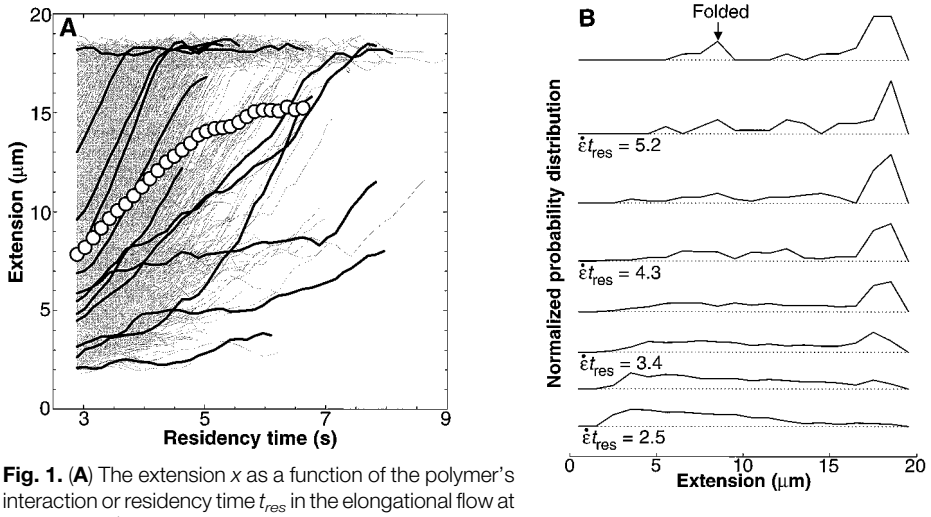

Fig. 1. (**A**) The extension x as a function of the polymer's interaction or residency time t_{res} in the elongational flow at $\dot{\varepsilon} = 0.86\ s^{-1}$ for 992 molecules. Several individual traces are highlighted. We also plotted the average extension $\langle x(t_{res})\rangle$ as open circles. Notice in particular, the large heterogeneity in the dynamics of these molecules. To slow down the dynamics, we used an aqueous sugar solution ($\eta = 41$ cP). We imaged those molecules whose center of mass started within 22 μm of the center line of the inlet channel. Within this region, the measured velocity gradient along the full length of the inlet ($\partial v_x/\partial x = -\dot{\varepsilon}$) was linear and within 2% of the measured velocity gradient along the outgoing axis ($\partial v_y/\partial y = \dot{\varepsilon}$). Because the fluid is incompressible ($\nabla\cdot\vec{v} = 0$) and it is a planar flow ($\partial v_z/\partial z = 0$), the molecules experienced a constant strain rate independent of position. Furthermore, the calibrated strain rate measured by tracking fluorescent beads agreed within 2% with the strain rate calculated from the motion of the center of intensity of individual DNA molecules. The data starts at $t_{res} > 0$, because the onset of elongational flow x_{onset} is 960 μm upstream from the stagnation point, whereas the edge of the imaging area x_{screen} is 86 μm upstream. The interaction time of the polymer with the applied velocity gradient before imaging is given by $t = \ln(x_{onset}/x_{screen})/\dot{\varepsilon}$. The raw extension data was smoothed by weighted averages with its nearest neighbor of $x_i = 0.21\ x_{i-1} + 0.58\ x_i + 0.21\ x_{i+1}$. (**B**) Time evolution of the probability distribution of molecular extension calculated from an ensemble of at least 40 individual molecules at $\dot{\varepsilon} = 0.86\ s^{-1}$. The secondary peak arises from molecules in a folded configuration (Fig. 2). Keuning's simulations of a bead-spring-bead model generated similar broadly shaped histograms (*33*), though such simulations are incapable of producing the secondary peak associated with folded configuration seen in the experimental data.

A polymer is said to "affinely" deform with the fluid if the molecular deformation equals the deformation of the surrounding fluid element. It has been suggested that when $\dot{\varepsilon} \gg 1/\tau_{relax}$, affine deformation becomes an increasingly valid approximation (*29*). In the simplest analysis, we note that $\langle x(t_{res})\rangle$ did not reach x_{steady} even after an accumulated fluid strain of $\varepsilon = \dot{\varepsilon} t_{res} \cong 5.7$, which corresponds to an $e^{5.7}$ or ~300-fold distortion of the fluid element (Fig. 3). For comparison, the required molecular distortion to fully extend stained λ-DNA is $L/R_G \cong 30$ where R_G, the radius of gyration, is 0.73 μm (*21*).

In part, this lack of affine deformation in $\langle x(t_{res})\rangle$ arises from the large variation in t_{onset}. Notwithstanding this variation which is intrinsically nonaffine, we wanted to know if molecules deform affinely once they start to stretch. To do so, we analyzed the dynamics of the master curve because it suppresses the variation in t_{onset} by computing $\langle \dot{x}(x)\rangle$ instead of $\langle \dot{x}(t_{res})\rangle$. At moderate strain rates, affine deformation is not expected, because there must be some slip between the polymer and the fluid to create the hydrodynamic force necessary to overcome the native elasticity of the polymer. Because there is no deformation for $\dot{\varepsilon} < \dot{\varepsilon}_c$, we plotted $\dot{\varepsilon}_{mol}$ versus $\dot{\varepsilon}_{fluid} - \dot{\varepsilon}_c$, where $\dot{\varepsilon}_c \cong 0.4/\tau_{relax}$. At lower $\dot{\varepsilon}$, the molecules are stretching near the theoretically expected limit (Fig. 4). At higher $\dot{\varepsilon}$, the data shows a marked departure, and it is clear that the affine deformation approximation breaks down. Furthermore, when plotted as $\dot{\varepsilon}_{mol}/(\dot{\varepsilon}_{fluid} - \dot{\varepsilon}_c)$ versus $(\dot{\varepsilon}_{fluid} - \dot{\varepsilon}_c)$, the data is decreasing at 0.86 s^{-1}. Thus, the data shows neither an absolute nor a fractional approach toward affine deformation at higher $\dot{\varepsilon}$ even after eliminating the large variation in t_{onset}. This failure arises from the introduction of intramolecular constraints (folds) which dramatically slow down the average dynamics. On the other hand, the subset of molecules in a dumbbell configuration stretched almost as fast as can be theoretically expected.

Our steady-state results are approximately characterized by a simple "dumbbell" model consisting of two beads connected by a spring based on the Marko-Siggia force law (Fig. 3B, solid line) (*20*). Previously, the steady-state extension of a tethered polymer in a uniform flow was well described by this model (*17*), and we developed a molecular understanding of the origin of this agreement based on simulations (*22*). An extrapolation of the model to $x = 0$ gives a critical strain rate of $\dot{\varepsilon}_c \tau_{relax} \cong 0.4$, which is near the theoretical value of 0.5 calculated from the Zimm model and by the numerical calculation of Larson and Magda (*3*). This value of $\dot{\varepsilon}_c \tau_{relax} \cong 0.4$ is less than the values of 3 to 8 seen in recent birefringence measurements of polystyrene solutions by Nguyen *et al.* (*9*).

To see if this model could self-consistently describe the dynamics of the master curve, we calculated the expected dynamics, using parameters determined from the steady-state

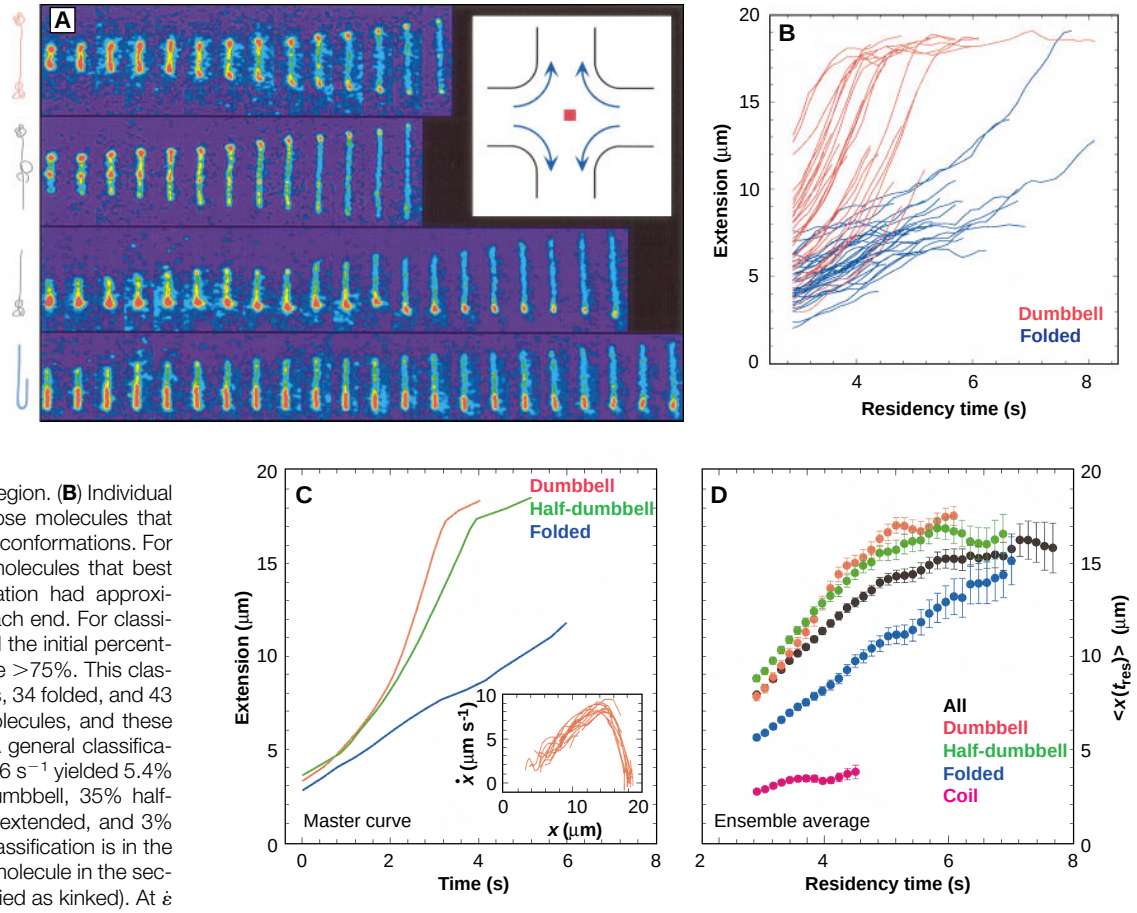

Fig. 2. Conformation-dependent rate of stretching: (**A**) Images of molecular configurations spaced every 0.13 s at the highest strain rate investigated ($\dot{\varepsilon} = 0.86\ s^{-1}$). We classified these configurations as (from top to bottom) dumbbell, kinked, half-dumbbell, and folded. The molecular extension of the last image in the first row is 13.9 μm. Sketches of possible molecular configurations are shown on the left. (**Inset**) A schematic illustration of the flow pattern where the red rectangle indicates the observation region. (**B**) Individual traces of x versus t_{res} for those molecules that best typify dumbbell or folded conformations. For classification purposes, the molecules that best typified a dumbbell configuration had approximately symmetric "coils" at each end. For classification as folded, we required the initial percentage of the folded section to be >75%. This classification yielded 30 dumbbells, 34 folded, and 43 half-dumbbells out of 992 molecules, and these molecules were reanalyzed. A general classification of all molecules at $\dot{\varepsilon} = 0.86\ s^{-1}$ yielded 5.4% kinked, 24% folded, 20% dumbbell, 35% half-dumbbell, 8.3% uniform, 5% extended, and 3% coils where precedence for classification is in the listed order (for example, the molecule in the second row of Fig. 2A was classified as kinked). At $\dot{\varepsilon} = 0.51 s^{-1}$, this classification yielded 3.7% kinked, 10% folded, 31% dumbbells, 33% half-dumbbells, 9.8% uniform, 3.7% extended, and 9.1% coils. A coil is a ball-shaped configuration that did not deform during the observation time. (**C**) Comparison of the "master curves" for dominant conformations. To obtain these curves, we integrated $\langle \dot{x}(x)\rangle$ versus x for those molecules that best typified each conformation where $\langle \dot{x}\ \langle x\rangle\rangle$ was calculated by binning the individual $\dot{x}(x)$ measurements every 0.5 μm. (**Inset**) The rate of extension $\dot{x}$ for each dumbbell molecule in Fig. 2B was calculated by a linear fit over five successive data points. (**D**) The average extension $\langle x\rangle$ as a function t_{res} for all of the data (black) and the different conformations (colors) for $\dot{\varepsilon} = 0.86\ s^{-1}$. Averages were calculated from at least 40 molecules except for the coiled configuration, which because of the limited number of coils and their lack of variability, was calculated from an ensemble of at least 10 molecules.

results. Whereas the predicted rate of extension is close to the measured dynamics for the dumbbell configuration, it overestimates the average measured dynamics (Fig. 4, inset). So, although this dumbbell model describes the steady-state extension, it fails to describe these simplified dynamics in which the large variation in t_{onset} is suppressed. Therefore, we expect difficulty in trying to predict the transient stress in the fluid by constitutive equations based on a simple dumbbell model (*2*). Given the nonaffine deformation, a term proportional to $-\dot{x}$ which can describe an "internal viscosity" might be added (*2*). Such a term is suggested by the measurements of η_E because it leads a dissipative component of the stress relaxation (*15*). Although a term proportional to $-\dot{x}$ can approximately compensate for the slower average dynamics, our data show that, in part, these slower dynamics arise from folded configurations which are meta-stable rather than arising from the monomer-monomer friction typically associated with internal viscosity. We note that there are additional terms besides $-\dot{x}$ that can lead to dissipative stresses (*30, 31*).

Given our measurements of the dynamic, steady-state, and ensemble-averaged properties of polymers in an elongational flow, we now compare our data to previous experimental and theoretical results. Atkins and Taylor measured the birefringence of λ-DNA in a similar planar elongational flow (Fig. 3B) (*8*). Our ability to select only those molecules that have reached steady-state extensions reveals a much sharper transition occurring at a lower $\dot{\varepsilon}_c\tau_{relax}$. As discussed above, the higher value of $\dot{\varepsilon}_c\tau_{relax}$ seen by birefringence occurred for synthetic polymers as well as for DNA (*9*). Evidently there is no direct correspondence between either x_{steady} or x_{bulk} and the birefringence at the stagnation point. Because birefringence measures orientation rather than extension, some disagreement would be expected based on the observed conformational features such as folds. However, folds would cause a premature saturation in birefringence with respect to x_{steady}. Our results highlight the difficulties in interpreting birefringence and other bulk measurements and suggest that this difficulty may be even greater for synthetic polymers, for which the larger ratio of L/R_G requires an even larger accumulated fluid strain than is needed to extend λ-DNA.

In contrast to previous light scattering results on synthetic polymers (*4, 5*), our data shows extensions significantly greater than ~2 R_G, though R_G, by definition, is always less than $x/2$. In general, the large difference between R_G and $x_{steady}/2$ is caused by the broad distribution in t_{res} for the population of molecules measured by light scattering. Hence, $x_{bulk}/2$, not $x_{steady}/2$, should be used for comparison. In addition, the highly asymmetric mass distribution of the most common conformation (half-dumbbell) would further reduce R_G. In particular, we directly calculated R_G from the image data for $\dot{\varepsilon}\tau_{relax} = 1.2$. A spatio-temporal average of this data yielded $R_G^{bulk} = 2.2$ μm, which is three times the equilibrium coil size [R_G = 0.73 μm (*21*)] but is much smaller than steady-state extension ($x_{steady} = 14.8$ μm) at this $\dot{\varepsilon}$. Thus, our results help explain the apparent discrepancy between light scattering and birefringence measurements.

Our results suggest that midpoint chain fracture in stagnation point flows does not imply that all chains are extended. The large variability in x (Fig. 1A) indicates that a number of molecules rapidly reach steady state. If we extrapolate our results to a $\dot{\varepsilon}$ of 100 times higher, it is these highly extended, early-stretching molecules that will experience a force large enough to fracture at or near their center. Nonetheless, because of the limited t_{res}, the number of such chains that are rapidly stretching and start stretching early is relatively small. Thus, only a fraction of the total number of chains fracture in agreement with the results of bulk experiments (*8, 11*), but this fracture of some chains does not imply that all chains are extended.

Rheologists often infer molecular deformation from bulk viscoelastic measurements (*2*). Given the data in Fig. 1, the known elasticity of DNA (*20*), and classical results in rheology (*2*), one can calculate the extensional stress $\sigma_E = n\langle x \cdot F(x)\rangle$ and the extensional viscosity $\eta_E = \sigma_E/\dot{\varepsilon}$ where n is density of molecules and $F(x)$ is the steady-state elasticity. However, because these molecules are in highly non-equilibrium configurations (Fig. 2A), it is inaccurate to use the steady-state elasticity for molecules at $\dot{\varepsilon} \gg 1/\tau_{relax}$. From this and the lack of a physically significant mean as described below, our results suggest difficulties with inferring an average conformation from bulk rheological measurements. Additionally, our results reveal problems with the use of the Peterlin approximation (*32*), in which $x^2(t_{res})$ is replaced by $\langle x^2(t_{res})\rangle$, to derive constitutive equations that predict bulk rheological measurements from a micromechanical or kinetic theory (*2*). The heterogeneity in our data that leads to the breakdown of the Peterlin approximation is also seen in Keunings' stochastic simulations of the finitely extensible dumbbell model (*33*). Although this simpli-

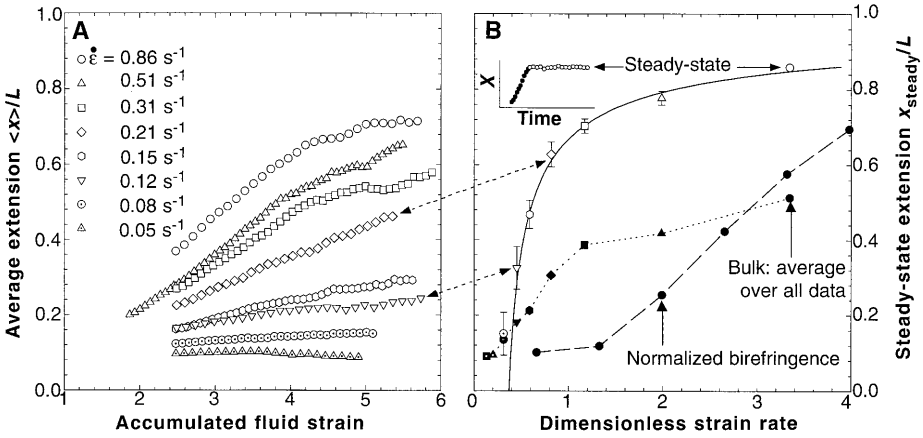

Fig. 3. (**A**) Fractional average extension $\langle x\rangle/L$ calculated from an ensemble of individual measurements as a function of the accumulated fluid strain $\varepsilon = \dot{\varepsilon}t_{res}$. The deformation of the surrounding fluid element is given by $\exp(\varepsilon)$. Averages were calculated from up to ~1000 individual molecules for the five highest strain rates and up to ~400 molecules at the lower strain rates depending on t_{res}. Averages for <40 molecules were not plotted. For $\dot{\varepsilon} = 0.51\ s^{-1}$, the stage was moved 100 μm up an inlet to observe the earlier time evolution. Note the similarity in the slope between the two highest $\dot{\varepsilon}$ implies the difference in magnitude of $\langle x\rangle/L$ probably arises more from a reduction in $\langle\dot{\varepsilon}t_{onset}\rangle$ than from an increase in $\dot{x}$ for the highest $\dot{\varepsilon}$. This supposition is verified by the analysis presented in Fig. 4. (**B**) The steady-state extension x_{steady} (open symbols) and "bulk" averaged extension x_{bulk} (closed symbols) as a function of the dimensionless strain rate $\dot{\varepsilon}\tau_{relax}$, where τ_{relax} is the longest relaxation time (*34*) or, more precisely, the slowest measured relaxation time from an extended state (*8, 26*). For the five highest $\dot{\varepsilon}$, x_{steady} was fit to a dumbbell model (solid line) with a worm-like spring (*20*) and two parameters: the contour length (L = 21.1 μm) of the stained DNA and the effective bead radius (R_{bead} = 0.16 μm). This value of L for stained λ-DNA is close to our previous measurement of L = 22 μm (*17*). Because of the large fluctuations at lower $\dot{\varepsilon}$, x_{steady} was calculated as average over all the data after the molecule reached the lower bound of the fluctuations about x_{steady}. x_{bulk} was determined by a spatio-temporal average over all measurements. The dashed line is the normalized birefringence data of dilute λ-DNA by Atkins and Taylor (*8*). The dashed arrows indicate the relationship between $\langle x(t_{res})\rangle$ and x_{steady} for the same $\dot{\varepsilon}$. Note, $\langle x(t_{res})\rangle$ does not reach x_{steady} within $\dot{\varepsilon}t_{res} \leq 5.7$ even though some individual molecules do (see inset). The symbol shape is preserved between plots and indicates $\dot{\varepsilon}$. (**Inset**) An individual molecule stretching to a steady-state value (open circles).

fied model of polymer dynamics based on kinetic theory yields histograms that are in semiquantitative agreement with our data (Fig. 1B), simulations with the Peterlin approximation in conjunction with kinetic theory lead to qualitatively different results.

To account for the excess stress measured by James and Saringer (*12*), Ryskin, Larson, Hinch, and King and James have developed theories based on different hypothesized molecular configurations (*16*, *31*). By direct observation of dumbbell, half-dumbbell, folded, and kinked conformations, we confirm the presence of conformations similar to those proposed. The presence of these conformations provides a qualitative explanation for the dissipative component of stress found in measurements of η_E. However, no one of the theories describes the complete range of observed conformations. Rather, the individual conformations assumed in these theories represent one of the several observed conformations.

From a theoretical point of view, the conformation-dependent dynamics implies that the commonly used approach of developing mean-field theories has an inherent disadvantage (*34*). The probability distribution is not a narrow distribution about a mean but rather a broad, oddly shaped distribution (Fig. 1B) because of several distinctly different dynamical processes (Fig. 2). Further, the differences in $\dot{x}$ and t_{onset} imply a sensitive dependence on the polymer's initial conformation when it enters the velocity gradient. Presumably, these variations arise directly from the multitude of accessible conformations at equilibrium where thermal fluctuations cause instantaneous deviations away from a spherically symmetric distribution. For instance, a polymer whose initial configuration has both ends on the same side of the center of mass and is subject to a $\dot{\varepsilon} \gg 1/\tau_{relax}$ would most likely become folded, because there is not enough time (τ_{relax}) for an end to move to the other side of the molecule. Variations similar to those in our experimental data have been observed in the simulations of Larson (*31*), Hinch (*16*), and Keunings (*33*).

Although we observe a sudden increase in the steady-state extension of polymers at a critical strain rate, our data indicates that the concept of a discrete and abrupt coil-stretch transition is limited to the steady state. Polymers do not undergo a simple, collective and simultaneous unwinding as soon as $\dot{\varepsilon} > \dot{\varepsilon}_c$. The mismatch between $\langle x(t_{res})\rangle$ and x_{steady} implies that the non-Newtonian properties of dilute polymer solutions in most practical elongational flows (where $\dot{\varepsilon}t_{res} < 5.5$) are dominated by the dynamic and not the steady-state properties. Our data should serve as a guide in developing improved microscopic theories for polymer dynamics and the bulk rheological properties of such solutions.

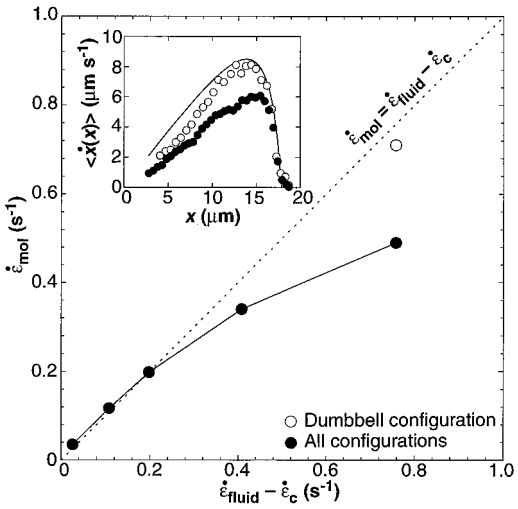

Fig. 4. A comparison between the rates of deformation of the fluid element ($\dot{\varepsilon}_{fluid} \equiv \dot{\varepsilon}$) and the polymer as characterized by the master curve. We subtract $\dot{\varepsilon}_c$, the experimentally determined critical strain rate, from the $\dot{\varepsilon}_{fluid}$ to account for the necessary difference between and $\dot{\varepsilon}_{fluid}$ and $\dot{\varepsilon}_{mol}$. This difference leads to the hydrodynamic force that stretches the polymer against its native elasticity. The master curve is used instead of $\langle x(t_{res})\rangle$, as it better represents the unwinding dynamics by suppressing the variation in t_{onset}. To define a molecule strain rate from the master curve, $\dot{\varepsilon}_{mol}$ was calculated from fitting $\langle \dot{x}(x)\rangle = \dot{\varepsilon}_{mol}\, x + b$ over the region where $\langle \dot{x}(x)\rangle$ is a linear function of x. As shown in the inset, this approximately linear behavior is seen for $x <$ 11.8 μm at $\dot{\varepsilon} = 0.86\ s^{-1}$. For the lower $\dot{\varepsilon}$, $\langle \dot{x}(x)\rangle$ was linear in x up to 5.2, 7.8, 8.8, and 10.2 μm in increasing order of $\dot{\varepsilon}$. If affine deformation becomes an increasingly valid approximation at higher $\dot{\varepsilon}$, then the data would line along the line described by $\dot{\varepsilon}_{mol} = \dot{\varepsilon}_{fluid} - \dot{\varepsilon}_c$ (dotted line). $\dot{\varepsilon}_{mol}$ determined for those molecules that best typify a dumbbell configuration is plotted as an open symbol (see Fig. 2C, inset). (**Inset**) $\langle \dot{x}(x)\rangle$ versus x for all molecules at $\dot{\varepsilon} = 0.86\ s^{-1}$ (filled circles) and molecules in the dumbbell configuration (open circles). The solid line represent the dynamics predicted by the dumbbell model using the values (R_{bead}, L) determined by the fit of x_{steady} to $\dot{\varepsilon}$ shown in Fig. 3B. More explicitly, we sum the hydrodynamic and entropic forces and set them to zero ($F_{total} = F_{hydro} - F_{spring} = 0$), where $F_{hydro} = 6\pi\eta R_{bead}(v_{fluid} - \dot{x}_{predicted}(x)/2)$, $v_{fluid} = 0.5\dot{\varepsilon}x$, and $F_{spring} = f(x/L)$ as given in (*20*). Because $\dot{x}_{predicted}$ is calculated at a given x, rather than a t_{res}, F_{total} is a function on only x and $\dot{\varepsilon}$ given R_{bead} and L from the fit to the steady-state data. We can then calculate the predicted rate of stretching of the total chain at each x to be $\dot{x}_{predicted} = 2(6\pi\nu R_{bead}v_{fluid} - F_{spring})/6\pi\eta R_{bead}$ (dashed line). Thus, this simple model overestimates the average dynamics although it agrees closely with the dynamics of molecules in the dumbbell configuration. The introduction of a term $(1 + \alpha)$ multiplying $\dot{x}_{predicted}$ in F_{hydro}, where $\alpha = 0.55$ approximately compensates for this overestimation of the dynamics at $\dot{\varepsilon} = 0.86\ s^{-1}$. Note that the variation in Fig. 4 away from $\dot{\varepsilon}_{mol} = \dot{\varepsilon}_{fluid} - \dot{\varepsilon}_c$ shows that this coefficient α is dependent on $\dot{\varepsilon}$.

REFERENCES AND NOTES

1. P. G. de Gennes, *J. Chem. Phys.* **60**, 5030 (1974).
2. R. G. Larson, *Constitutive Equations for Polymer Melts and Solution* (Buttersworths, New York, 1988); R. B. Bird, C. F. Curtiss, R. C. Armstrong, O. Hassager, *Dynamics of Polymeric Liquids* (Wiley, New York, ed. 2, 1987), vol. 2.
3. R. G. Larson and J. J. Magda, *Macromolecules* **22**, 3004 (1989).
4. M. J. Menasveta and D. A. Hoagland, *ibid.* **24**, 3427 (1991).
5. K. A. Smith, E. W. Merrill, L. H. Peebles, S. H. Banijamali, *Colloq. Int. CNRS* **233**, 341 (1975); J. L. Lumley, *Phys. Fluids* **20**, s64 (1977).
6. A. Keller and J. A. Odell, *Colloid Polym. Sci.* **263**, 181 (1985).
7. G. G. Fuller and L. G. Leal, *Rheol. Acta* **19**, 580 (1980); C. A. Cathey and G. G. Fuller, *J. Non-Newtonian Fluid Mech.* **34**, 63 (1990); P. N. Dunlap and L. G. Leal, *ibid.* **23**, 5 (1987).
8. E. D. T. Atkins and M. A. Taylor, *Biopolymers* **32**, 911 (1992). To plot the data in Fig. 3B, we normalized birefringence by the maximum birefringence and multiplied their $\dot{\varepsilon}$ by $\tau_1 = 0.067$ s, where we determined τ_1 for λ-DNA by scaling $\tau_1 = 0.046$ s reported by L. C. Klotz and B. H. Zimm [*J. Mol. Biol.* **72**, 779 (1972)] for T7-DNA in a creep recovery experiment and scaled for the slight difference in length between T7 and λ-DNA with a scaling exponent of 1.66 (*35*). This value of $\tau_1 = 0.067$ s is in agreement, after scaling for length, with $\tau_1 = 0.058$ to 0.068 s from intrinsic viscosity [L. C. Klotz and B. H. Zimm, *J. Mol. Biol.* **72**, 779 (1972)], light scattering [K. S. Schmitz and R. Percora, *Biopolymers* **14**, 521 (1975)], birefringence [D. S. Thompson and S. J. Gill, *J. Chem. Phys.* **47**, 5008 (1967)], and flow dichroisim experiments [P. R. Callis and N. Davidson, *Biopolymers* **8**, 379 (1969)]. For a comparison of our τ_{relax} to τ_1, see (*26*).
9. T. Q. Nguyen, G. Yu, H.-H. Kausch, *Macromolecules* **28**, 4851 (1995).
10. Recent experiments by Nguyen *et al* (*9*) exhibited the same saturation, but when the probe region is moved toward the outlet, the birefringence increased, which suggests that polymers had not reached equilibrium. However, S. P. Carrington and J. A. Odell [*J. Non-Newtonian Fluid Mech.* **67**, 269 (1996)] argue that this is a concentration-dependent effect.
11. J. A. Odell, A. Keller, Y. Rabin, *J. Chem. Phys.* **88**, 4022 (1988); J. A. Odell, A. Keller, A. J. Muller, *Colloid Polym. Sci.* **270**, 307 (1992); J. A. Odell and M. A. Taylor, *Biopolymers* **34**, 1483 (1994). See also H. R. Reese and B. H. Zimm [*J. Chem. Phys.* **92**, 2650 (1990)], which focuses on DNA fracture through an orifice.
12. D. F. James and J. H. Saringer, *J. Fluid Mech.* **97**, 655 (1980).
13. V. Tirtaatmadja and T. Sridhar, *J. Rheol.* **37**, 1081 (1993).
14. D. F. James and T. Sridhar, *ibid.* **39**, 713 (1995).
15. S. H. Spiegelberg and G. H. McKinely, *J. Non-Newtonian Fluid Mech.* **67**, 49 (1996); N. V. Orr and T. Sridhar, *ibid.*, p. 77.
16. E. J. Hinch, *ibid.* **54**, 209 (1994).
17. T. T. Perkins, D. E. Smith, R. G. Larson, S. Chu, *Science* **268**, 83 (1995).
18. Some molecules (<5%) are fractured, possibly during the mixing of the DNA into the high-viscosity buffer, but a visual inspection of the light intensity and size can generally rule out these smaller molecules.
19. S. B. Smith, L. Finzi, C. Bustamante, *Science* **258**, 1122 (1992); A. Vologodskii, *Macromolecules* **27**, 5623 (1994).
20. J. F. Marko and E. D. Siggia, *Macromolecules* **28**, 8759 (1995); C. Bustamante, J. F. Marko, E. D. Sig-

gia, S. Smith, *Science* **265**, 1599 (1994). Their analytic approximation for the elasticity is given by $Fp/k_BT = 0.25*(1 - x/L)^{-2} - 0.25 + x/L$, where F is the force applied across the ends, p is the persistence length, and k_BT is the thermal energy.
21. D. E. Smith, T. T. Perkins, S. Chu, *Macromolecules* **29**, 1372 (1996).
22. R. G. Larson, T. T. Perkins, D. E. Smith, S. Chu, *Phys. Rev. E* **55**, 1794 (1997).
23. Following the example of W. D. Volkmuth and R. H. Austin [*Nature* **358**, 600 (1992)], we made our flow cells by etching silicon wafers with KOH and anionically bonding Pyrex coverslips to the silicon to seal the top surface of the channels. Vertical side walls along the inlet and outlet channels were achieved by rotating the pattern by 45° to the crystal axis [C. Hu and S. Kim, *Appl. Phys. Lett.* **29**, 582 (1976)]. To generate the flow, we used a syringe pump (Isco model 100 D) which was temperature-stabilized at 22.7°C. A ~100:1 fluid shunt bypassing the flow cell was used to operate the pump at flow rates >40 μl/min. The velocity field was calibrated by tracking fluorescent beads near the stagnation point and showed $v_y = \dot{\varepsilon}\, y$, confirming that a uniform elongational flow had been achieved. Our imaging and digitization system was the same as previously described (*17*), except we used a water immersion objective (Zeiss 40× C-APO NA 1.2) and stroboscopically illuminated the DNA to eliminate the blurring of the image due to camera lag. Our measurements of the equilibrium coil size generally did not yield $2\,R_G$ but something slightly larger due to blooming in the camera. Once the chain is extended about two times the equilibrium size, the blooming is reduced and the measurements correspond closely to the actual extension. We stained the λ-DNA (New England Biolabs) with YOYO-1 (Molecular Probes) at a dye:base-pair ratio of 1:4 for >1 hour. The experiment was performed in a high viscosity (η = 41 centipoise) buffer consisting of 10 mM tris-HCl, 2 mM EDTA, 10 mM NaCl, 4% β-mercaptoethanol, ~50 μg/ml glucose oxidase (Boehringer Mannheim), ~10 μg/ml catalase (Boehringer Mannheim), ~18% (w/w) glucose and ~40% (w/w) sucrose. The viscosity of each solution was measured in a temperature-stabilized viscometer and adjusted as needed. The flow cell was mounted on a copper block and stabilized to 22.7° ± 0.2°C.
24. To prevent any predeformation of the polymer before entering the elongational flow, we used a cross-slot flow cell with channels 650 μm wide and 220 μm deep and imaged the polymers at the center of depth of the channel (z_{center} = 110 μm) where the applied shear ($\dot{\gamma} \equiv \partial v_x/\partial z$) was negligible. Because of the mismatch in the index of refraction of the immersion fluid (water) and the high viscosity buffer, we determined z_{center} by measuring the velocity of fluorescent beads in the inlet as a function of depth and fitting this velocity to a parabolic, Poiseuille velocity field. Because of their finite size ($R_G \cong 0.7$ μm), polymers at z_{center} still experienced some shear. For our highest strain rate ($\dot{\varepsilon} = 0.86\ s^{-1}$), the corresponding reduced shear rate in the inlet was $\dot{\gamma}\tau_{relax} = 0.5$, which is below the expected onset of deformations (*2*). We observed no deformation of the polymers in the inlet at $\dot{\varepsilon} = 0.86\ s^{-1}$, but a doubling of the flow rate led to modest (~4 μm) predeformation of some molecules. We used 25-mm-long inlet channels, which allowed any molecule deformed upon entering the flow cell sufficient time (>8 τ_{relax}) to relax back to equilibrium before entering the elongational flow.
25. At the lower strain rates, there were not distinct, well preserved conformations, but the large variation t_{onset} still occurred. The polymers had the general appearance of a dumbbell configuration subject to a large fluctuations in extension and shape.
26. We determined τ_{relax} = 3.89 s by averaging the relaxation of 14 individual, highly extended molecules. The relaxation time we report is from a fit over the region where $x/L < 0.3$ to $\langle x(t)x(t)\rangle = c \exp(-t/\tau_{relax}) - 2\,R_G$, where τ_{relax}, c, and R_G were free parameters. This is directly related to the relaxation of the stress in the fluid via $\sigma_E = n\,\langle x \cdot F(x)\rangle$, because in the limit of small deformation, $F(x)$ is linear in x and this yields $\sigma_E(t) \sim \langle x(t)x(t)\rangle$. Thus, our characterization of τ_{relax} via stress relaxation is made in the region ($x/L < 0.3$) where $\tau_{relax} \cong \tau_1$ because the contribution of higher order relaxation modes should be negligible (*2*). When scaled to η = 1 centipoise and for the change in length caused by staining, our τ_{relax} for unstained, λ-DNA in water is 0.061 s (*8*). This analysis does not take into account any possible changes in persistence length. No change in solvent quality was measured between sucrose and glycerol viscosity-enhanced aqueous buffered solution used for the measurements of τ_{relax} and τ_1, respectively (*35*). Our τ_{relax} reported here is different than relaxation time determined from $\langle x(t)\rangle = c \exp(t/\tau) - R_G$, which yields τ = 6.2 s, and is the relaxation time we reported in an earlier experiment where the DNA was tethered to a bead (*35*).
27. The longer DNA molecules were concatemers of λ-DNA (up to 250 μm). We were unable to systematically investigate the dynamics of longer molecules, because we did not have an adequately monodisperse sample and could not independently measure the length of individual molecules.
28. The results presented here should not be generalized to polymers in a mixed elongational and shearing flow or to polymers in an elongational flow that were presheared. Our data indicates that the processes involved in the diverse dynamics arise from the variation in t_{onset} and from internal configurations (that is, folds). In mixed flows, a large fraction of the molecules are partially extended because of shearing, and this effect may eliminate some of the internal constraints that led to the observed dynamics.
29. S. Daoudi and F. Brochard, *Macromolecules* **11**, 751 (1978); P. G. de Gennes, *Scaling Concepts in Polymer Physics* (Cornell Univ. Press, Ithaca, NY, 1979); E. J. Hinch, *Phys. Fluids* **20**, 522 (1977).
30. J. M. Rallison, *J. Non-Newtonian Fluid Mech.* **68**, 61 (1997). For simulations of longer chains, see P. S. Doyle, E. S. G. Shaqfeh, and A. P. Gast [*J. Fluid Mech.* **334**, 251 (1997)].
31. G. Ryskin, *Phys. Rev. Lett.* **59**, 2059 (1987); *J. Fluid Mech.* **178**, 423 (1987); R. G. Larson, *Rheol. Acta* **29**, 371 (1990); D. H. King and D. F. James, *J. Chem. Phys.* **78**, 4749 (1983).
32. A. Peterlin, *Makromol. Chem.* **44**, 338 (1961).
33. R. Keunings, *J. Non-Newtonian Fluid Mech.* **68**, 85 (1997).
34. B. H. Zimm, *J. Chem. Phys.* **24**, 269 (1956); P. E. Rouse, *ibid.* **21**, 1272 (1953).
35. T. T. Perkins, S. R. Quake, D. E. Smith, S. Chu, *Science* **264**, 822 (1994).

36. We thank G. Fuller, D. Hoagland, R. Larson, R. Pecora, and B. Zimm for helpful discussions and J. Shott for generous aid in lithographic design. Supported in part by grants from the U.S. Air Force Office of Scientific Research, NSF, and the Human Frontiers Foundation and by an endowment established by Theodore and Frances Geballe. We acknowledge the generous assistance of J. Spudich, including support through NIH grant GM33289 to J. Spudich. D.E.S. was supported by a fellowship from the Program in Mathematics and Molecular Biology at the University of California, Berkeley, through NSF grant DMS 9406348. S.C. was supported in part by a Guggenheim fellowship during the course of this work.

18 February 1997; accepted 8 May 1997

Surface Stress in the Self-Assembly of Alkanethiols on Gold

Rüdiger Berger,* Emmanuel Delamarche, Hans Peter Lang, Christoph Gerber, James K. Gimzewski, Ernst Meyer, Hans-Joachim Güntherodt

Surface stress changes and kinetics were measured in situ during the self-assembly of alkanethiols on gold by means of a micromechanical sensor. Self-assembly caused compressive surface stress that closely followed Langmuir-type adsorption kinetics up to monolayer coverage. The surface stress at monolayer coverage increased linearly with the length of the alkyl chain of the molecule. These observations were interpreted in terms of differences in surface potential. This highly sensitive sensor technique has a broad range of applicability to specific chemical and biological interactions.

Molecular and biomolecular layers are scientifically appealing for a wide range of potential applications (*1*, *2*). Alkanethiols, which are known to self-organize into well-ordered, densely packed films, represent a model molecular system for controlling surface properties (*3*, *4*). These self-assembled monolayers (SAMs) are used in applications such as microcontact printing (*5*) and voltametric microsensors (*6*), and they have recently been applied to molecular host-guest recognition (*7*).

There is little information available on the mechanical properties of SAMs, particularly concerning the nature of surface stress in films during the formation process, because it is difficult to follow the structural evolution of monolayer self-assembly. One recent approach (*8*) used scanning tunneling microscopy to infer the growth kinetics of alkanethiol SAMs indirectly from snapshot images obtained at various coverages. Here, we used micromechanical sensors to gather quantitative data on surface stress changes that develop during the self-assembly process of HS-

R. Berger and H. P. Lang, IBM Research Division, Zürich Research Laboratory, CH-8803 Rüschlikon, Switzerland, and Institute of Physics, University of Basel, CH-4056 Basel, Switzerland.
E. Delamarche, Ch. Gerber, J. K. Gimzewski, IBM Research Division, Zürich Research Laboratory, CH-8803 Rüschlikon, Switzerland.
E. Meyer and H.-J. Güntherodt, Institute of Physics, University of Basel, CH-4056 Basel, Switzerland.
*To whom correspondence should be addressed.